

One-dimensional theoretical analysis on charged-particle transports in a decaying plasma with an initial plasma–electrode gap

Xin-Li Sun(孙鑫礼), Yao-Ting Wang(汪耀庭), Lan-Yue Luo(罗岚月), Zi-Ming Zhang(张子明), Meng-Long Zhang(张梦龙), He-Ping Li(李和平), Dong-Jun Jiang(姜东君), and Ming-Sheng Zhou(周明胜)

Citation: Chin. Phys. B, 2025, 34 (**11**): 115201. DOI: 10.1088/1674-1056/ade385
http://cpb.iphy.ac.cn; http://iopscience.iop.org/cpb

What follows is a list of articles you may be interested in

Pulse interval tunable terahertz radiation from electron beam-plasma interactions

Die Jian(简蝶), Jie Cai(蔡杰), Li-Qi Han(韩立琦), Xing-Yu Zhao(赵兴宇), Han Wen(温寒), and Jin-Qing Yu(余金清)
Chin. Phys. B, 2025, 34 (**10**): 105201. DOI: 10.1088/1674-1056/add67a

Observation of Weibel magnetic fields in laser-produced interpenetrating flows

Chuanqi Shi(施川奇), Dawei Yuan(袁大伟), Wei Sun(孙伟), Yapeng Zhang(张雅芃), Zhijie Qiu(邱志杰), Huigang Wei(魏会冈), Zhe Zhang(张喆), Xiaohui Yuan(远晓辉), and Gang Zhao(赵刚)
Chin. Phys. B, 2025, 34 (**1**): 015203. DOI: 10.1088/1674-1056/ad94e4

Velocity analysis of supersonic jet flow in double-cone ignition scheme

Zhong-Yuan Zhu(朱仲源), Cheng-Long Zhang(张成龙), and Ying-Jun Li(李英骏)
Chin. Phys. B, 2024, 33 (**6**): 065203. DOI: 10.1088/1674-1056/acc1d4

Model of self-generated magnetic field generation from relativistic laser interaction with solid targets

Rui Yan(严睿), De-Bin Zou(邹德滨), Na Zhao(赵娜), Xiao-Hu Yang(杨晓虎), Xiang-Rui Jiang(蒋祥瑞), Li-Xiang Hu(胡理想), Xin-Rong Xu(徐新荣), Hong-Yu Zhou(周泓宇), Tong-Pu Yu(余同普), Hong-Bin Zhuo(卓红斌), Fu-Qiu Shao(邵福球), and Yan Yin(银燕)
Chin. Phys. B, 2024, 33 (**5**): 055203. DOI: 10.1088/1674-1056/ad333f

Theoretical analyses on the one-dimensional charged particle transport in a decaying plasma under an electrostatic field

Yao-Ting Wang(汪耀庭), Xin-Li Sun(孙鑫礼), Lan-Yue Luo(罗岚月), Zi-Ming Zhang(张子明), He-Ping Li(李和平), Dong-Jun Jiang(姜东君), and Ming-Sheng Zhou(周明胜)
Chin. Phys. B, 2023, 32 (**9**): 095201. DOI: 10.1088/1674-1056/ace033

One-dimensional theoretical analysis on charged-particle transports in a decaying plasma with an initial plasma–electrode gap

Xin-Li Sun(孙鑫礼), Yao-Ting Wang(汪耀庭), Lan-Yue Luo(罗岚月), Zi-Ming Zhang(张子明), Meng-Long Zhang(张梦龙), He-Ping Li(李和平)†, Dong-Jun Jiang(姜东君), and Ming-Sheng Zhou(周明胜)

Department of Engineering Physics, Tsinghua University, Beijing 100084, *China*

(Received 9 April 2025; revised manuscript received 31 May 2025; accepted manuscript online 11 June 2025)

An analytical model for describing the charged-particle transport in a wall-confined laser-induced decaying plasma is established under an external electrostatic field, focusing on the effects of the initial plasma–electrode gap (IPEG) that exists in applications such as laser isotope separation. This newly developed analytical model is validated by particle-in-cell simulations and the experimental scaling relation, and can also be reduced to its previously published counterpart that did not consider IPEGs. Based on this analytical model, the influences of different IPEG spacings on the characteristics of the whole ion extraction process are studied. The results show that the ion extraction ratios at the endpoints of the first and second stages both decrease with increasing IPEG spacing, while the corresponding time durations for the first two stages show a non-monotonous variation trend. The specific ion extraction time, defined as the ion extraction time per unit mass to comprehensively characterize the ion extraction efficiency, increases generally with the increase of IPEG spacing. This study not only provides further insight into the fundamental physical processes in a wall-bounded decaying plasma under an externally applied electrostatic field, but also offers useful theoretical guidance for optimal designs of geometrical and operating parameters in laser isotope separation processes.

Keywords: decaying plasma, charged-particle transport, effect of plasma–electrode gap, theoretical analysis, PIC simulation

PACS: 52.30.–q, 52.35.Fp, 52.50.Qt, 28.60.+s

DOI: 10.1088/1674-1056/ade385 **CSTR:** 32038.14.CPB.ade385

1. Introduction

Wall-confined decaying plasmas are widely used in many applications, such as plasma immersion ion implantation[1–3] and the ion extraction process of laser-induced plasmas.[4–7] In this paper, we focus on the characteristics of the charged-particle transport, especially ion extraction fluxes, during a laser-induced decaying plasma under an externally applied electrostatic field in the context of laser isotope separation. In both fundamental and applied research, the ion extraction flux and ion extraction time during plasma decay are two key parameters for characterizing the performance of the laser isotope separation technique. The parameters are comprehensively determined by the spatiotemporal evolutions of electrode sheath expansion, ion-acoustic rarefaction wave (IRW) propagation, as well as the parameters (e.g., electron and ion number densities and electric potential) in the core plasma region confined between two solid electrodes. As shown in Fig. 1, resulting from heating of solid metal or metal alloys by an electron beam, metallic atomic vapor forms with evaporation at the liquid metal surface and moves upward with expansion due to a low chamber pressure (e.g., on the magnitude of 10^{-2} Pa, or even 10^{-3} Pa). A weakly ionized plasma is then generated by irradiation from an intense laser beam. Next, the ions are extracted from the core plasma region and collected on the electrodes under an externally applied electrostatic or electromagnetic field within a short time. One of the intrinsic features, as well as a major challenge, of the ion extraction process is the electrode sheath, especially at high initial plasma densities (e.g., on the magnitude of 10^{11} cm^{-3}), which screens the externally imposed electrostatic field and significantly reduces the ion extraction flux, resulting in a longer ion extraction time and lower ion extraction efficiency.

In order to improve the ion extraction efficiency, many studies have been reported, including by varying the electrode configurations (e.g., M-type,[8–11] Π-type[12–14]), by using alternating electric fields (e.g., radio-frequency electric field,[15–18] alternatively biased electric field[19]) or even with the aid of magnetic fields[20–22] to collect the target ions on two electrodes simultaneously or for weakening the shielding effect of the electrode sheath. Among the three major theoretical research methods including analytical analyses,[5,23–25] fluid simulations[26,27] and particle-in-cell (PIC) simulations,[28,29] the analytical method can present clear physical images of the ion extraction process with reasonable assumptions and avoid heavy computational burdens, particularly for PIC simulations with higher plasma densities and/or larger electrode gap spacings. According to the previous analytical analyses, a typical ion extraction process in a laser-induced decaying plasma under an external electrostatic field consists of three

†Corresponding author. E-mail: liheping@tsinghua.edu.cn

© 2025 Chinese Physical Society and IOP Publishing Ltd. All rights, including for text and data mining, AI training, and similar technologies, are reserved.

successive stages,[25] among which much attention has been paid to the second stage, i.e., the sheath expansion and IRW propagation stage. For example, the early theoretical work by Chen[5] focused on rapid sheath expansion and established an analytical model considering the balance among the Langmuir flux, Bohm flux and additional flux due to the sheath motion. As for the influences of IRW, Allen and Andrews[30] theoretically predicted the profiles of velocity, density and electric potential in the plasma region perturbed by the propagation of IRWs. Later, Murakami and Nishihara[24] established a sheath dynamic model considering the relative velocity between the sheath edge motion and IRW front propagation, i.e., under supersonic and subsonic sheath expansion states. While Khrabrov *et al.*[31] considered the interaction of two opposing IRWs and its influence on the evolution of the plasma parameters theoretically and numerically in a one-dimensional (1-D) collisionless plasma initiated between two parallel absorbing walls.

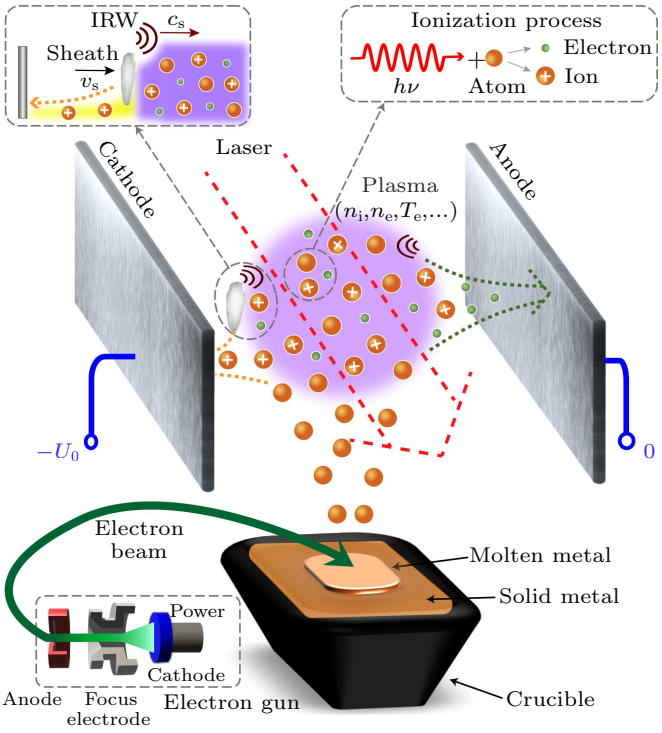


Fig. 1. Schematic of the charged-particle transport in a laser-induced decaying plasma considering various factors. The symbols n_i, n_e, T_e, v_s and c_s represent ion density, electron density, electron temperature, sheath motion speed and ion-acoustic speed, respectively.

Although the duration of the first stage, i.e., electron oscillation and matrix sheath extraction stage, is not as long as that of the second stage, a much higher level of ion extraction flux than that of Langmuir flux[32] and a considerable ion extraction ratio[25] occur in this stage. Consequently, increasing attention has been paid to this stage. Chen *et al.*[28] investigated the electron oscillation process at the beginning of the ion extraction process with the aid of theoretical analyses and PIC simulations, and pointed out for the first time that the existence of electron oscillation and IRW propagation resulted in a non-zero ion flux to the anode. Later, Chen *et al.*[33] and Wang *et al.*[18] presented a quantitative description of the electron oscillation frequency and a criterion on the initial plasma density for the initial electron temperature effects on the ion extraction time. Wang *et al.*[25] also derived formulae for the ion extraction fluxes to the cathode and anode, respectively, during the first stage, which were well validated by PIC simulations. Based on previous research from the same group, an analytical model considering all the three stages was firstly established in Refs. [25,34], in which the 1-D spatiotemporal evolutions of the densities and fluxes of ions, electric potentials, and electrode sheath positions in the whole plasma decay process under an external electrostatic field could be predicted analytically when the gap space between two parallel metallic plates is initially fully occupied by a laser-induced plasma; this was also validated by comparisons with PIC simulation results.

From the perspective of industrial applications, there is always a gap between the laser-induced plasma and the electrode at the beginning of the ion extraction process, which is the so-called initial plasma–electrode gap (IPEG). Appropriate IPEG spacing is generally indispensable, as too large a gap would decrease ion extraction efficiency, while too small or no gap spacing could lead to the deposition of neutral particles on the electrodes, which negatively affects the product purity.[35] Although the effect of the IPEG on the ion extraction characteristics has been taken into account in many previous experimental studies during laser-induced decaying plasmas,[12,19,36–38] the influences of IPEGs have not been considered in the previously published theoretical analyses, e.g., Ref. [25]. Therefore, this paper aims to establish an analytical model for describing the whole 1-D ion extraction process considering the IPEG effect in a decaying plasma under an electrostatic field. The organization of this paper is as follows: brief descriptions of the physical model and PIC simulation code are presented in Section 2, following a review of current research in Section 1; then, in Section 3, the 1-D analytical model for the whole ion extraction process considering the IPEG effect is derived and validated by PIC simulations and the experimental scaling relation; next, discussions of influences of different IPEG spacings on the charged-particle transport characteristics are presented in Section 4; and the major conclusions are presented in Section 5 accompanied by a brief discussion on future research.

2. Physical model and PIC simulation code

In this study, a 1-D ion extraction system considering IPEG spacing is studied, as depicted in Fig. 2, where the electrode gap spacing is L, while the electric potentials imposed on the anode ($x = L$) and the cathode ($x = 0$) are fixed at 0 and

$-U_0$, respectively. A laser-induced plasma containing singly-charged argon ions (Ar^+) and electrons (e^-) is distributed uniformly between two parallel metallic electrodes. A vacuum gap with width d exists between the plasma and the electrode. Since this study focuses on the fundamental charged-particle transport during ion extraction from a decaying plasma and different plasmas with different ion masses have no intrinsic influences on the ion extraction characteristics, we still use argon plasma here as a counterpart of the case with no IPEGs.[25] Thus, three basic assumptions are employed as follows: (i) collisionless plasma resulting from a species mean free path exceeding the system characteristic length significantly under the typical operating pressures, i.e., on the magnitude of 10^{-3} Pa; (ii) complete charged-particle absorption at electrode surfaces once arriving at the electrodes; and (iii) initial Maxwellian velocity distributions for both ions and electrons, characterized by temperatures $T_{i,0}$ and $T_{e,0}$, respectively.

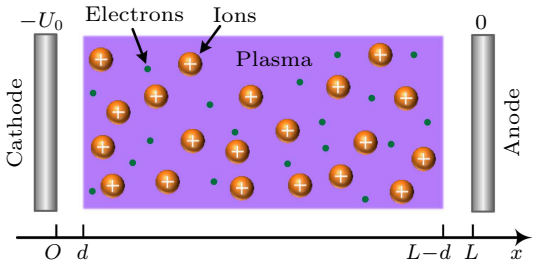


Fig. 2. Schematic of the 1-D ion extraction system considering the existence of an IPEG.

Table 1. Parameters for the typical case studied in this paper.

Physical parameters	Value
Electrode spacing [L (cm)]	2.0
Initial plasma–electrode gap spacing [d (cm)]	0.1
Externally applied voltage [$-U_0$ (V)]	−400
Initial plasma number density [n_0 (10^{16} m^{-3})]	2.5
Initial electron/ion temperature [$T_{e,0}/T_{i,0}$ (eV)]	0.5/0.02

In this study, a 1-D code, EDIPIC,[39] is used to simulate the ion extraction process. EDIPIC is a well-developed code for PIC simulation of decaying plasmas and has been verified and validated in literature.[28,31,39] To ensure sufficiently high accuracy while minimizing computational consumption, some key simulation parameters are set as follows according to previous studies:[28] the grid size is set to 0.1 times the Debye length, i.e., $\Delta x = 0.1\lambda_D$, and the time step is set to ensure that the electrons do not transit across one grid in one time step, i.e., $v_e\Delta t < \Delta x$, while the initial number of macroparticles in each grid is set to be 256, i.e., $N_P = 256$. A brief discussion on the simulation method and parameter selection can be found in Appendix A. In addition, the operating parameters for a typical case are listed in Table 1, which were selected based on previous studies.[13,18,28,29,39–41] Since the ratio of the total IPEG spacing to the system characteristic length ($2d/L$) in reported experimental studies ranges from 8% to 20%,[12,19,36–38] the value of the IPEG spacing, $d = 0.1$ cm, is chosen for the typical case in Table 1 corresponding to a value of $2d/L = 10\%$.

3. Derivation and validation of the analytical model

Before deriving the analytical model for the whole ion extraction process, all the physical parameters are normalized using the same method as that described in Ref. [25]. The dimensionless form of the physical parameters are defined as follows:

$$S = \frac{s}{\lambda_D}, \quad X = \frac{x}{\lambda_D}, \quad \Lambda = \frac{L}{\lambda_D}, \quad D = \frac{d}{\lambda_D},$$
$$T = \omega_{pi}t, \quad U = \frac{u}{c_s}, \quad N = \frac{n}{n_0}, \quad \Psi_0 = \frac{eU_0}{kT_{e,0}}, \tag{1}$$

where s, x, L, d, t, u, n and U_0 refer to the sheath thickness, spatial position, electrode spacing, IPEG spacing, time, macroscopic ion velocity, number density of particles and externally applied voltage before normalization, respectively, and the basic physical parameters used for normalization include λ_D (Debye length), ω_{pi} (ion plasma frequency), c_s (ion-acoustic speed), e (elementary charge), k (Boltzmann constant), $T_{e,0}$ (initial electron temperature) and n_0 (initial ion number density). The left side of each formula in Eq. (1) is the corresponding dimensionless form of the preceding parameters. Correspondingly, the ion flux can be normalized by (n_0c_s) and denoted using the symbol Γ.

3.1. Theoretical analyses of the whole ion extraction process considering the effect of the IPEG

Although the whole ion extraction process can still be generally divided into three successive stages as reported in Ref. [25], the effects of the IPEG on the electron oscillation, matrix sheath formation, Langmuir sheath expansion and IRW propagation cannot be ignored during the decaying of plasmas. In this subsection, an analytical model for the whole ion extraction process considering the effect of IPEG is derived theoretically.

3.1.1. Effect of IPEG on the electron oscillation and matrix sheath formation in the first stage

Firstly, due to the existence of IPEGs, the matrix sheath thickness on the cathode side (denoted as $S_{m,ca}$) can be expressed as[18]

$$S_{m,ca} = \begin{cases} \Psi_0/D, & D \geq D_c, \\ \text{RealRoot}\left[-D^3 + 3D^2 S_{m,ca} \right. \\ \left. +3DS_{m,ca}^2 + S_{m,ca}^3 = 6\Psi_0 S_{m,ca}\right], & D < D_c, \end{cases} \tag{2}$$

where $D_c = (\Psi_0)^{1/2}$ is the critical distance indicating whether the electrons can overlap the IPEG in the oscillation process or not. Using a similar method to that presented in Ref. [18], the matrix sheath thickness on the anode side (denoted as $S_{m,an}$)

can be written as (a detailed derivation can be found in Appendix B)

$$S_{\mathrm{m,an}} = S_{\mathrm{m,ca}} - \frac{2\Psi_0}{2D + S_{\mathrm{m,ca}}}. \tag{3}$$

After the ions cover the IPEGs near the electrodes, both the ion density and ion flux to the cathode suddenly increase, and the temporal evolution of the ion density near the cathode is consistent with the case of the IPEG-free model,[2,25] i.e.,

$$N_{\mathrm{ca}} = \frac{2}{T^2 + 2}. \tag{4}$$

As shown in Fig. 3, the time evolutions of the ion number density near the cathode with different IPEGs using Eq. (4) are well validated by the PIC simulation results where the ion density probes are all located at $x = 0.01$ cm, which is close enough to the cathode surface. Based on the preceding results, the expressions for the ion fluxes to the cathode ($\Gamma_{\mathrm{m,ca}}$) and anode ($\Gamma_{\mathrm{m,an}}$), as well as for the end time of the first stage ($T_{\mathrm{m,end}}$), can be obtained using the similar methods as those used for the case with no consideration of the IPEGs,[25] which can be expressed as

$$\Gamma_{\mathrm{m,ca}}(T) = -(S_{\mathrm{m,ca}} + D) \times \frac{\mathrm{d}}{\mathrm{d}T}\mathrm{Hyp2F1}\left(\frac{1}{2}, \frac{3}{4}, \frac{7}{4}, -\frac{1}{4}T^2\left(T^2+4\right)\right), \tag{5}$$

$$\Gamma_{\mathrm{m,an}}(T) = -S_{\mathrm{m,an}} \times \frac{\mathrm{d}}{\mathrm{d}T}\mathrm{Hyp2F1}\left(\frac{1}{2}, \frac{3}{4}, \frac{7}{4}, -\frac{T^2\left(T^2+4\right)}{4}\left(\frac{S_{\mathrm{m,an}}}{D + S_{\mathrm{m,ca}}}\right)^{\frac{4}{3}}\right), \tag{6}$$

$$T_{\mathrm{m,end}} = \sqrt{2\sqrt{4\left[\frac{3}{4}\left(D + S_{\mathrm{m,ca}}\right)\right]^{4/3} + 1} - 2}, \tag{7}$$

where Hyp2F1 is a Gaussian hypergeometric function.

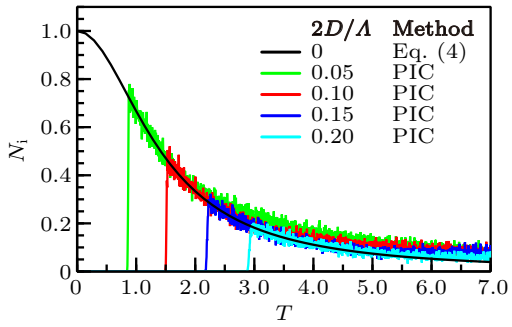


Fig. 3. Temporal evolutions of the ion number density near the cathode under different IPEG spacings predicted by PIC simulations and comparison with the calculated result using Eq. (4) for the case with no IPEGs.

Secondly, with the existence of IPEGs, additional time for ions to cover the initial plasma–electrode gap spacing is necessary before the ion extraction flux occurs, as shown in Fig. 3. The times for the ions to occupy the IPEG near the cathode and the anode are denoted as $T_{\mathrm{arr,ca}}$ and $T_{\mathrm{arr,an}}$, respectively, which can be derived as follows: In the vicinity of the cathode, the advance of the ion front can be approximated by the model of uniformly accelerated motion of a singly-charged ion, i.e.,

$$D_{\mathrm{ca}} = D - \frac{\Psi_0}{2D}T^2 \rightarrow T_{\mathrm{arr,ca}} = \sqrt{\frac{2}{\Psi_0}}D, \tag{8}$$

where D_{ca} is the dimensionless distance between the ion front and the cathode surface. The calculated values of D_{ca} using Eq. (8) are well validated by the PIC simulations with a maximum relative discrepancy of 4.2%, as shown in Fig. 4. In our opinion, one of the major sources of the discrepancy between the PIC modelling results and the theoretically predicted values using Eq. (8) for $T_{\mathrm{arr,ca}}$ may be due to the preceding assumption of the uniform acceleration of ions with a constant electric field of (Ψ_0/D), while the PIC modelling shows that the electric field at the ion front is a little bit smaller than (Ψ_0/D) during the actual electron oscillation process; consequently, the value of $T_{\mathrm{arr,ca}}$ predicted by Eq. (8) is somewhat lower than that of the PIC simulations.

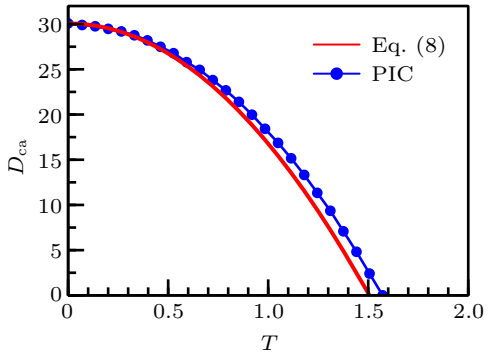


Fig. 4. Comparison of the estimated values of D_{ca} using Eq. (8) with those of the PIC simulation results.

Since after an external electrostatic field is imposed on the plasmas, the electric field near the cathode is much higher than that near the anode, a longer time is needed for the ions to occupy the IPEG on the anode side than that on the cathode side. If we assume that the ion density inside the ion sheet remains uniform, and thus, an averaged ion density obtained by conservation of particles is used to approximate the actual ion density profile, the electric field near the anode can be obtained based on the Poisson equation and the corresponding boundary conditions using a similar method to that presented in Ref. [18]. Thus, when $T < T_{\mathrm{arr,ca}}$, we have

$$E_{\mathrm{an}} = -\frac{S_{\mathrm{m,ca}}\left(D_{\mathrm{an}} - D_{\mathrm{ca}} - 2\Lambda\right)}{2\Lambda} + \frac{\Psi_0\left(-D + D_{\mathrm{an}} - 2\Lambda + S_{\mathrm{m,ca}}\right)}{\Lambda\left(2D + S_{\mathrm{m,ca}}\right)} - \frac{2\Psi_0^2}{\Lambda\left(2D + S_{\mathrm{m,ca}}\right)^2}, \tag{9a}$$

and when $T > T_{\mathrm{arr,ca}}$, we have

$$E_{\mathrm{an}} = -\frac{S_{\mathrm{m,ca}}\left(D_{\mathrm{an}} - 2\Lambda\right)}{2\Lambda} + \frac{\Psi_0\left(-D + D_{\mathrm{an}} - 2\Lambda + S_{\mathrm{m,ca}}\right)}{\Lambda\left(2D + S_{\mathrm{m,ca}}\right)} - \frac{2\Psi_0^2}{\Lambda\left(2D + S_{\mathrm{m,ca}}\right)^2}$$

$$-\frac{D+S_{\mathrm{m,ca}}}{2\Lambda}\int_{T_{\mathrm{arr,ca}}}^{T}\Gamma_{\mathrm{ca}}\left(T'\right)\mathrm{d}T', \tag{9b}$$

where D_{an} is the dimensionless distance between the ion front and the anode surface, while Γ_{ca} is the ion flux to the cathode. Therefore, the governing equation for D_{an} can be written as

$$\frac{\mathrm{d}^2 D_{\mathrm{an}}}{\mathrm{d}T^2} = -E_{\mathrm{an}}\left(T, D_{\mathrm{an}}\right). \tag{10}$$

Introducing Eq. (9) into Eq. (10), the variation of D_{an} with time can be obtained; and the time for the ions to occupy the IPEG near the anode, $T_{\mathrm{arr,an}}$, is just the time when D_{an} approaches zero. For the typical case listed in Table 1, the calculated value of $T_{\mathrm{arr,an}}$ using Eqs. (9) and (10) is 83.0 ns, while the PIC simulation result is 107.3 ns. Here, we hope to emphasize the following. Firstly, in our opinion, one of the major sources of such discrepancy between the theoretically predicted and PIC-simulated values of $T_{\mathrm{arr,an}}$ results from the assumption of a uniform ion density distribution inside the ion sheet in the preceding theoretical analysis. Thus, the theoretically predicted electric field near the anode and the ion advancement rate toward the anode are both over-estimated, leading to a lower theoretically predicted value of $T_{\mathrm{arr,an}}$ than that calculated by the PIC simulations. In order to obtain a more accurate estimation for $T_{\mathrm{arr,an}}$, a spatiotemporal evolution model for the ion density that agrees better with the actual ion distribution inside the ion sheet is preferred, which will be further studied in our future work. Secondly, although the relative discrepancy between the theoretically predicted value and the PIC modeling result is high (about 22.7%), the value of $T_{\mathrm{arr,an}}$ obtained from Eqs. (9) and (10) is still on the same magnitude as that of the PIC simulations, and the results presented in Fig. 5 in Subsection 3.2 will show that such discrepancy has no significant impact on the whole ion extraction characteristics.

3.1.2. Effect of IPEG on Langmuir sheath expansion and IRW propagation in the second and third stages

In the second and third stages of the extraction process, although the physical images of the Langmuir sheath expansion and the IRW propagation are qualitatively the same as those in the IPEG-free case (Eqs. (19), (21)–(27) in Ref. [25]), the existence of IPEGs will have effects on some key time points related with the Langmuir sheath expansion and the IRW propagation including the starting time points of the second stage ($T_{\mathrm{m,end}}$) and the third stage (T_{dis}), the end time of the supersonic sheath expansion state ($T_{\mathrm{sup,end,ca}}$), the starting point of IRW-C and IRW-A, as well as the time point when the IRW-A arrives at the anode surface ($T_{\mathrm{pm,end}}$), which influences the ion extraction fluxes in these two stages. In detail, considering the IPEGs, the evolution of the Langmuir sheath thickness in the supersonic expansion state starting from the initial conditions of $S = D + S_{\mathrm{m,ca}}$ and $T = T_{\mathrm{m,end}}$ can be expressed as

$$S(T) = \left[\left(S_{\mathrm{m,ca}}+D\right)^3 + \frac{4\sqrt{2}}{3}\Psi_0^{3/2}\left(T - T_{\mathrm{m,end}}\right)\right]^{1/3}. \tag{11}$$

Therefore, the time point at the end of the supersonic sheath expansion, $T_{\mathrm{sup,end,ca}}$, and the corresponding sheath thickness, $S_{\mathrm{sup,end,ca}}$, with $\mathrm{d}S/\mathrm{d}T = 1$ can be written as

$$\begin{aligned} T_{\mathrm{sup,end,ca}} &= T_{\mathrm{m,end}} + \frac{3}{4\sqrt{2}\Psi_0^{3/2}}\left[S_{\mathrm{sup,end,ca}}^3 - \left(S_{\mathrm{m,ca}}+D\right)^3\right], \\ S_{\mathrm{sup,end,ca}} &= \sqrt{\frac{4\sqrt{2}\Psi_0^{3/2}}{9}}. \end{aligned} \tag{12}$$

Then, subsonic sheath expansion occurs starting from the conditions of $S_0 = S_{\mathrm{sup,end,ca}}$ and $T_0 = T_{\mathrm{sup,end,ca}}$ when the IRW near the cathode (IRW-C) exceeds the sheath edge and advances toward the bulk plasma, while the IRW near the anode (IRW-A) excited at the position (Λ–D–$S_{\mathrm{m,an}}$) at time point $T_{\mathrm{m,end}}$ is also propagating toward both the anode and the bulk plasma until it encounters the Langmuir sheath edge, after which comes the third stage. Considering the IPEGs, the time point at which IRW-A arrives at the anode ($T_{\mathrm{pm,end}}$), as well as the relationship between the moment of IRW-A reaching the sheath edge (T_{dis}) and the corresponding sheath thickness at this time point (S_{dis}), can be written as

$$T_{\mathrm{pm,end}} = T_{\mathrm{m,end}} + D + S_{\mathrm{m,an}}, \tag{13}$$

$$S_{\mathrm{dis}} = \Lambda - D - S_{\mathrm{m,an}} - T_{\mathrm{dis}} + T_{\mathrm{m,end}}. \tag{14}$$

Based on the foregoing discussions, the ion extraction fluxes during the whole ion extraction process considering the effects of the IPEGs are summarized in Table 2. It can be seen clearly that the formulae listed in Table 2 can be reduced to their counterparts in the IPEG-free model[25] with $D = 0$, which, to some extent, validates the theoretical model developed in this study.

3.2. Validation of the analytical model

To further validate the theoretical model developed in this study considering the effect of the IPEGs, the ion fluxes to the cathode and anode during the whole ion extraction process predicted by the analytical model (Table 2) are compared with the PIC simulation results for the typical case listed in Table 1. As shown in Fig. 5, the theoretically predicted ion extraction fluxes agree well with the PIC simulation results. When 90% of ions are extracted theoretically, 88.2% of ions are extracted according to the PIC simulations with a relative discrepancy of 1.8%. To further validate the reliability of the analytical model obtained in this study (Table 2), the following tests are conducted:

(i) If we define the ion extraction time (t_{ext}) as the time point with 90% of ions extracted from the bulk plasma, variations of the calculated ion extraction ratios by the PIC simulations (R_{ext}) at the time point corresponding to the analytically predicted ion extraction time ($t_{ext,analytical}$) are shown in Fig. 6(a) under different ratios of the total IPEG spacings to the system characteristic length ($2D/\Lambda$) ranging from 0 to 20%, which covers most cases reported in experiments.[12,19,36–38] It is seen that the modeling results are close to the theoretically preset value of 90% with a maximum discrepancy of 2.3%.

(ii) With the following experimental scaling relation for the ion extraction time:[37]

$$\frac{t_{ext,scale}}{t_{ext,ref}} = \left(\frac{U_0}{U_{0,ref}}\right)^{-0.81}\left(\frac{L_{pl}}{L_{pl,ref}}\right)^{1.40}\left(\frac{n_0}{n_{0,ref}}\right)^{0.56}, \quad (15)$$

where $t_{ext,scale}$, U_0, L_{pl}, n_0 represent the scaled ion extraction time, externally applied voltage, plasma width, and initial plasma density before normalization, respectively, while the variables with the subscript "ref" represent the values corresponding to the reference case as listed in Table 1. As shown in Fig. 6(b), the ion extraction times predicted by the analytical model and those calculated by Eq. (15) both decrease as the IPEG spacing increases with a maximum relative discrepancy of 14.0%. Since the scaling relation in Ref. [37] has a relative error of 15% with experimental data, such a level of discrepancy is acceptable.

(iii) With a fixed value of $2D/\Lambda = 10\%$, the analytically predicted ion extraction times ($t_{ext,analytical}$) also agree well with the corresponding scaled values from Eq. (15), i.e., $t_{ext,scale}$, with a maximum relative discrepancy of 13.6% by changing the initial operating values of U_0, L_{pl}, n_0, as shown in Fig. 6(c).

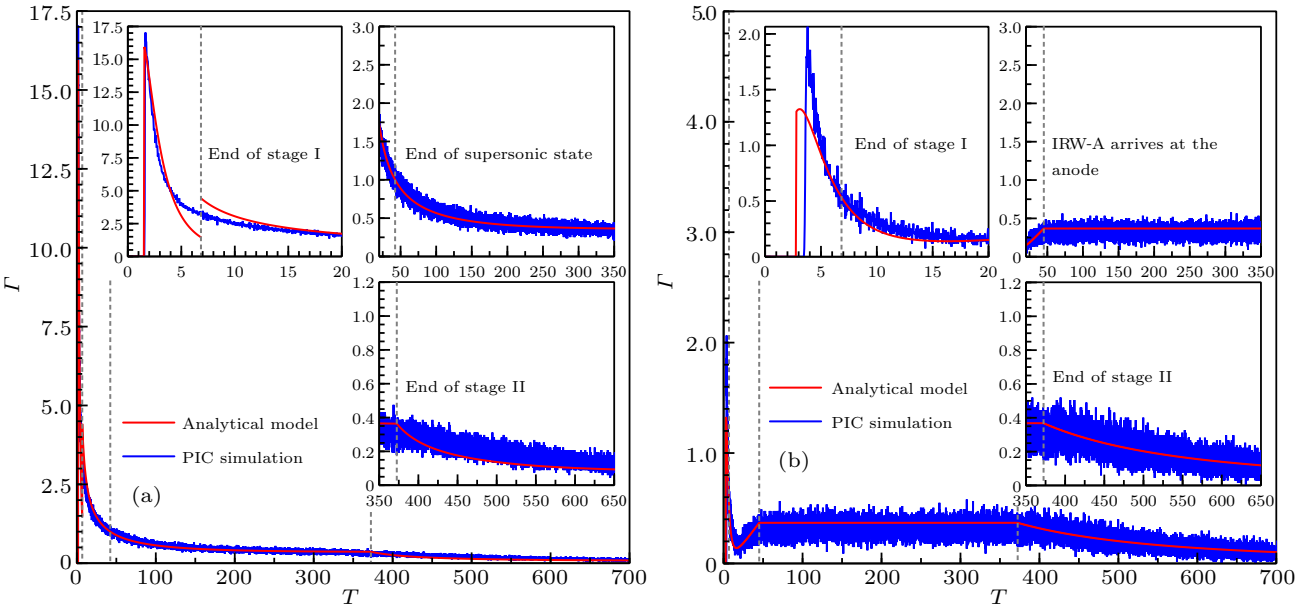


Fig. 5. Comparisons of the ion extraction fluxes to (a) the cathode and (b) anode between the theoretically predicted and the PIC simulated results for the typical case listed in Table 1.

Table 2. Analytical model describing the whole ion extraction process considering the effects of the IPEGs.

	Cathode	Anode
Stage I	$T_{arr,ca} = \sqrt{\frac{2}{\Psi_0}D}$ $\Gamma_{m,ca} = -(S_{m,ca}+D)\frac{d}{dT}\mathrm{Hyp2F1}\left(\frac{1}{2},\frac{3}{4},\frac{7}{4},-\frac{1}{4}T^2\left(T^2+4\right)\right)$ $T_{m,end} = \sqrt{2\sqrt{4\left[\frac{3}{4}\left(D+S_{m,ca}\right)\right]^{4/3}+1}-2}$	$T_{arr,an} = \mathrm{RealRoot}\left[D_{an}(T)=0\right]$, $\frac{d^2D_{an}}{dT^2} = -E_{an}(T,D_{an})$ $\Gamma_{m,an} = -S_{m,an}\frac{d}{dT}\mathrm{Hyp2F1}\left(\frac{1}{2},\frac{3}{4},\frac{7}{4},-\frac{T^2\left(T^2+4\right)}{4}\left(\frac{S_{m,an}}{D+S_{m,ca}}\right)^{4/3}\right)$
Stage II	Supersonic state: $\Gamma_{ca} = \frac{4\sqrt{2}}{9}\frac{\Psi_0^{3/2}}{S^2} = \frac{dS}{dT}$ $T_{sup,end,ca} = T_{m,end} + \frac{3}{4\sqrt{2}\Psi_0^{3/2}}\left(S_{sup,end,ca}^3 - (S_{m,ca}+D)^3\right)$, $S_{sup,end,ca} = \left(\frac{4\sqrt{2}\Psi_0^{3/2}}{9}\right)^{1/2}$ Subsonic state: $\Gamma_{ca} = \frac{4\sqrt{2}}{9}\frac{\Psi_0^{3/2}}{S^2} = \exp(\xi-1)\left(\frac{dS}{dT}+1-\xi\right)$, $\xi = \frac{S-S_{sup,end,ca}}{T-T_{sup,end,ca}}$ $T_{dis} = \Lambda - D - S_{m,an} - S_{dis} + T_{m,end}$, $\frac{4\sqrt{2}}{9}\frac{\Psi_0^{3/2}}{S_{dis}^2} = \exp(\xi-1)\left(\frac{dS}{dT}+1-\xi\right)$, $\xi = \frac{S_{dis}-S_{sup,end,ca}}{T_{dis}-T_{sup,end,ca}}$	Before IRW-A arriving at the anode: $\Gamma_{an} = \frac{\left(T_{pm,end}-T\right)\Gamma_{m,an}(T)+\left(T-T_{m,end}\right)\exp(-1)}{T_{pm,end}-T_{m,end}}$, $T_{pm,end} = T_{m,end}+D+S_{m,an}$ After IRW-A arriving at the anode: $\Gamma_{an} = \exp(-1)$
Stage III	$\Gamma_{ca} = \frac{4\sqrt{2}}{9}\frac{\Psi_0^{3/2}}{S^2} = N\left(\frac{dS}{dT}-U\right)$, $U = \frac{S-S_{sup,end,ca}}{T-T_{sup,end,ca}} - \frac{\Lambda-S}{T_{dis}-T_{m,end}}$ $N = \exp\left(\frac{\Lambda-\left(T-T_{sup,end,ca}+S_{sup,end,ca}\right)}{T_{dis}-T_{m,end}}-1\right)$	$\Gamma_{an} = \left(\frac{T-T_{dis}}{T_{dis}-T_{m,end}}+1\right)^{-2}\exp(-1)$

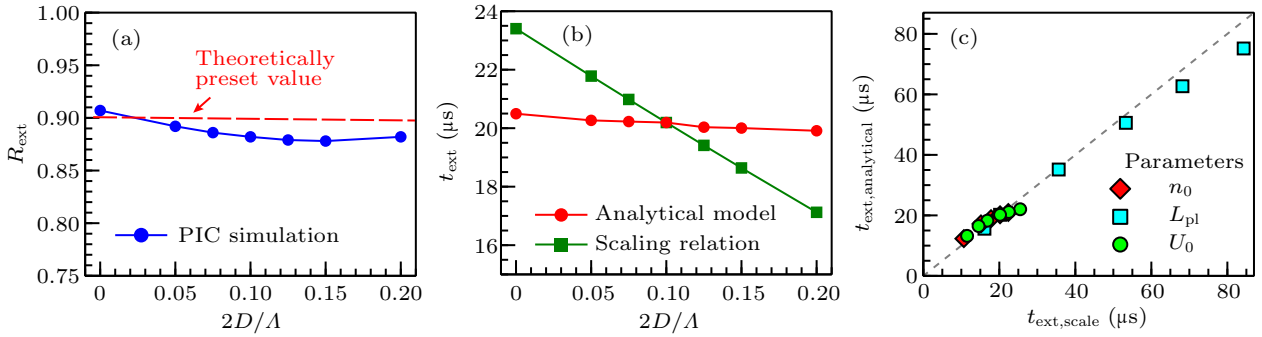


Fig. 6. (a) Variations of the calculated ion extraction ratios by the PIC simulations (R_{ext}) at the time points corresponding to the theoretically predicted ion extraction time ($t_{ext,analytical}$), (b) comparison of the theoretically predicted ($t_{ext,analytical}$) and experimentally scaled ($t_{ext,scale}$) ion extraction times under different values of $(2D/\Lambda)$, and (c) comparisons between $t_{ext,analytical}$ and $t_{ext,scale}$ with a fixed value of $(2D/\Lambda) = 10\%$ under the operating parameter ranges of $n_0 = 8\times10^{15}$–3×10^{16} m^{-3} (red rhombus), $L_{pl} = 1.5$–5.0 cm (cyan square) and $U = 300$–800 V (green circle), where the dashed line represents the cases with equal values of $t_{ext,analytical}$ and $t_{ext,scale}$.

4. Discussions concerning the effect of IPEG spacing on the ion extraction characteristics

In this section, the influences of the IPEG spacing on the ion extraction characteristics are discussed based on the analytical model obtained in Section 3. The case listed in Table 1 is still selected as the reference case, and thus, the corresponding parameters characterizing the ion extraction process, e.g., the end time of the first stage ($T_{m,end}$) and the second stage (T_{dis}), the sheath thickness at the end time of the second stage (S_{dis}), are used as the reference values. While, for other cases, the operating parameters except for the value of IPEG spacing are also the same as those listed in Table 1.

4.1. Effect of IPEG spacing on the end times of the first and second stages

Variation of the relative value of the end time of the first stage ($T_{m,end}$) under different IPEG spacings is shown in Fig. 7. Since the value of $(D + S_{m,ca})$ decreases at first and then increases with the increase of the total IPEG spacing and reaches its local minimum value at $D = (\Psi_0)^{1/2}$ (a detailed derivation can be found in Appendix C), the value of $T_{m,end}$ shows a nonmonotonic variation trend according to Eq. (7).

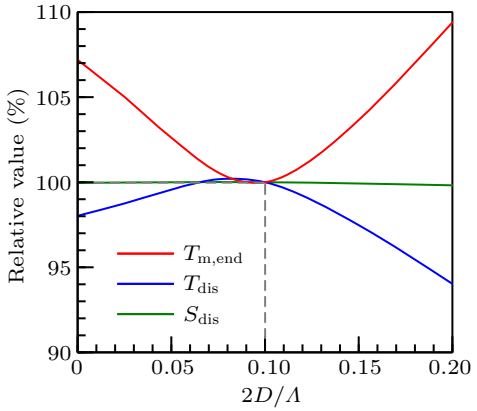


Fig. 7. Variations of $T_{m,end}$, T_{dis} and S_{dis} with the IPEG spacing. The relative values are based on the corresponding values of the case listed in Table 1.

As shown in Fig. 7, a similar variation trend also exists for the end time of the second stage (T_{dis}) with an increase of the total IPEG spacing, which results from a comprehensive influence of the IPEG spacing (D), the initial matrix sheath thickness on the anode side ($S_{m,an}$), the end time of the first stage ($T_{m,end}$) and the sheath thickness at the end of the second stage (S_{dis}) according to Eq. (14). Among the foregoing factors, the value of $(D + S_{m,an})$ shows a nonmonotonic variation trend with the increase of the total IPEG spacing and a local minimum peak appears near $D = (\Psi_0)^{1/2}$ (seen also in Appendix C), while the change of $T_{m,end}$ is less significant compared with $(D + S_{m,an})$ by comparing Figs. 7 and C2, and the variation of S_{dis} is negligible (Fig. 7). Consequently, the term of $(D + S_{m,an})$ plays a major role in determining the nonmonotonic variation trend of the end time of the second stage (T_{dis}) under different IPEGs.

4.2. Effect of IPEG spacing on the ion extraction ratios at the end of the first and second stages

In this section, the variables of r_1 and r_2 are denoted as the ion extraction ratios at the end of the first and second stages, respectively. Since the number of remaining ions in the Langmuir sheath at the end of the first stage is much smaller than that in the initial matrix sheath,[25] r_1 can be approximated as

$$r_{1,approx} = \frac{S_{m,ca} + S_{m,an}}{\Lambda - 2D}, \tag{16}$$

when ignoring the remaining ions in the Langmuir sheath. The comparison of r_1 obtained from the original analytical model (Table 2) and the approximate expression [Eq. (16)] is shown in Fig. 8. It is seen that both of the calculated values of r_1 decrease with an increase in the IPEG spacing with a maximum relative discrepancy of 25.0%. The variation trend of r_1 can be explained based on Eq. (16) as follows: With the increase of D, the decreasing effect of $(S_{m,ca} + S_{m,an})$ is much more significant than the increasing effect of $(\Lambda - 2D)^{-1}$ (e.g., for the typical case in Table 1, with an increase of ΔD =0.1, $(S_{m,ca} + S_{m,an})$ decreases by 0.43%, while $(\Lambda - 2D)^{-1}$ only increases by 0.04%), thus, the comprehensive effect of $(S_{m,ca} + S_{m,an})$ and $(\Lambda - 2D)$ leads to a decrease of r_1 with the increase of IPEG spacing.

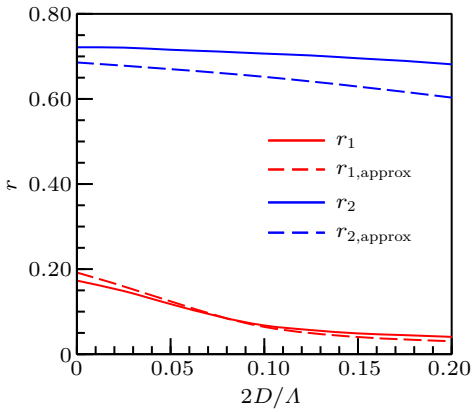


Fig. 8. Variations of ion extraction ratios at the end of the first and second stages obtained from the original analytical model and the corresponding approximated expressions.

Similarly, assuming a uniform density profile in the bulk plasma and ignoring the remaining ions in the Langmuir sheath at the end of the second stage,[25] r_2 can be approximated as

$$r_{2,\mathrm{approx}} = 1 - \frac{\Lambda - S_{\mathrm{dis}}}{\Lambda - 2D} \exp\left(\frac{S_{\mathrm{dis}} - S_{\mathrm{sup,end,ca}}}{T_{\mathrm{dis}} - T_{\mathrm{sup,end,ca}}} - 1\right). \quad (17)$$

The variations of r_2 obtained from the original analytical model (Table 2) and the approximate formula [Eq. (17)] are also shown in Fig. 8 with the same decreasing trend and a maximum relative discrepancy of 11.5%. Since the decreasing effect of $[-(\Lambda - 2D)^{-1}]$ is more obvious than the increasing effects of the exponential term and of $(\Lambda - S_{\mathrm{dis}})$ (e.g., for the typical case in Table 1, with an increase of ΔD =0.1, the value of $[-(\Lambda - 2D)^{-1}]$ decreases by 0.04%, while the exponential term only increases by 0.003% and the change of $(\Lambda - S_{\mathrm{dis}})$ is less than 3×10^{-6}), the value of r_2 is mainly determined by the factor of $(\Lambda - 2D)$, and also decreases with the increase of the IPEG spacing.

4.3. Effect of IPEG spacing on the ion extraction time and specific ion extraction time

The analytical model presented in Table 2 shows that the ion extraction time is comprehensively determined by the end time of the second stage, the number of remaining ions to be extracted and the ion extraction flux in the third stage. Generally, an earlier end time of the second stage, a smaller number of ions remaining at the end of the second stage, and/or larger ion extraction flux in the third stage will lead to a shorter ion extraction time. Considering the variation trend of T_{dis} with the IPEG spacing as shown in Fig. 7: (i) On the left part of the local maximum point, with the increase of the IPEG spacing, both the decrease in the number of remaining ions to be extracted at the end time of the second stage and the increase in $(T_{\mathrm{dis}} - T_{\mathrm{m,end}})$ which leads to an increase in the ion extraction flux during the third stage play dominant roles in determining the ion extraction time; consequently, less time is required for extracting the remaining ions, and thus, resulting in a decrease of the total ion extraction time. (ii) While, on the right part of the local maximum point, the earlier end of the second stage primarily contributes to the decrease in the total ion extraction time as the IPEG spacing increases. Therefore, the ion extraction time (T_{ext}) generally decreases with increasing IPEG spacing, as shown in Fig. 9.

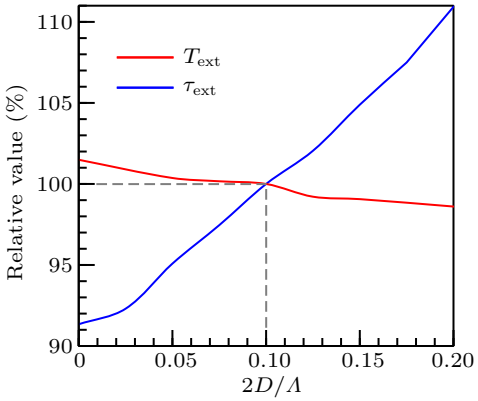


Fig. 9. Variations of the ion extraction time (T_{ext}) and the specific ion extraction time (τ_{ext}) with the IPEG spacing. The relative values are based on the corresponding value of the case listed in Table 1.

When the electrode gap spacing is fixed, an increase in the IPEG spacing indicates a reduction of the initial bulk plasma volume, i.e., a decrease of the initial total number of ions. Therefore, it is not sufficient to evaluate the efficiency accurately and comprehensively by merely using the parameter of ion extraction time. Thus, the concept of "specific ion extraction time", which is defined as the ion extraction time per unit mass, is introduced in this section and expressed as

$$\tau_{\mathrm{ext}} = \frac{T_{\mathrm{ext}}}{\Lambda - 2D}. \quad (18)$$

Based on Eq. (18), with the increase of the IPEG spacing (D), although the ion extraction time (T_{ext}) decreases, while simultaneously the initial number of ions also decreases significantly, i.e., the value of $(\Lambda - 2D)^{-1}$ increases significantly, and plays an important role in determining the value of τ_{ext}. For example, for the typical case listed in Table 1, when the value of $(2D/\Lambda)$ increases from 10% to 20%, the value of T_{ext} decreases by 1.4%, while the initial number of ions decreases by 11.1%. Therefore, the specific ion extraction time increases with the increase of the IPEG spacing, as shown in Fig. 9. In our opinion, in terms of actual applications, on the one hand, the specific ion extraction time is more appropriate to evaluate the efficiency of the ion extraction process when considering the existence of the IPEGs. A shorter specific ion extraction time means that less time is required to extract ions per unit mass, which indicates a higher ion extraction efficiency. On the other hand, it is essential to comprehensively consider the requirements for the higher ion extraction efficiency and the lower deposition of neutral particles on the electrodes with an optimized IPEG spacing.

In summary, the effect of the IPEG spacing on the key parameters discussed in this section can be summarized as listed in Table 3, where the symbols $D_{\mathrm{c,ca}}$, $D_{\mathrm{c,an}}$, $N_{\mathrm{rem,II}}$ and Γ_{III} denote the critical points of $(D+S_{\mathrm{m,ca}})$ and $(D+S_{\mathrm{m,an}})$, as shown in Fig. B1, the number of remaining ions to be extracted at the end of the second stage, and the averaged ion extraction flux in the third stage, respectively.

Table 3. Effect of the IPEG spacing on the key parameters discussed in Section 4.

Parameter	Dominant factor	Variation trend with increasing IPEG spacing
$T_{\mathrm{m,end}}$	$D+S_{\mathrm{m,ca}}$	Decreasing (↓) if $D<D_{\mathrm{c,ca}}$ Increasing (↑) if $D>D_{\mathrm{c,ca}}$
T_{dis}	$-(D+S_{\mathrm{m,an}})$	Increasing (↑) if $D<D_{\mathrm{c,an}}$ Decreasing (↓) if $D>D_{\mathrm{c,an}}$
r_1	$S_{\mathrm{m,ca}}+S_{\mathrm{m,an}}$	Decreasing (↓)
r_2	$-(\Lambda-2D)^{-1}$	Decreasing (↓)
T_{ext}	$N_{\mathrm{rem,II}}$, Γ_{III}	Decreasing (↓) if $D<D_{\mathrm{c,an}}$
	T_{dis}	Decreasing (↓) if $D>D_{\mathrm{c,an}}$
τ_{ext}	$(\Lambda-2D)^{-1}$	Increasing (↑)

5. Concluding remarks and future research

In this paper, a 1-D theoretical analysis of the charged-particle transport in a wall-confined laser-induced decaying plasma with the consideration of an initial plasma–electrode gap (IPEG) under an externally applied electrostatic field is conducted. The major conclusions are as follows.

(1) A 1-D analytical model for the whole ion extraction process is established in a laser-induced decaying plasma confined between two parallel metallic electrodes under an electrostatic field with a special focusing on the IPEG effect. This newly developed analytical model is validated by PIC modeling and the experimental scaling relation, and can be reduced to its counterpart with no consideration of the IPEGs reported in our previous study when the IPEG spacing becomes zero. Based on this analytical model, the spatiotemporal evolution of the 1-D wall-confined decaying plasma, as well as the sheath expansion and IRW propagation during the whole ion extraction process with the consideration of the IPEG, is illustrated in Fig. 10.

(2) With the increase of the IPEG spacing, the ion extraction ratios at the end of the first stage (r_1) and the second stage (r_2) both decrease, while the end time of the first stage ($T_{\mathrm{m,end}}$) and the second stage (T_{dis}) show nonmonotonic variation trends mainly due to the nonmonotonic variation trends of the sum of IPEG spacing and matrix sheath thickness on the cathode side $(D+S_{\mathrm{m,ca}})$ and that on the anode side $(D+S_{\mathrm{m,an}})$, respectively.

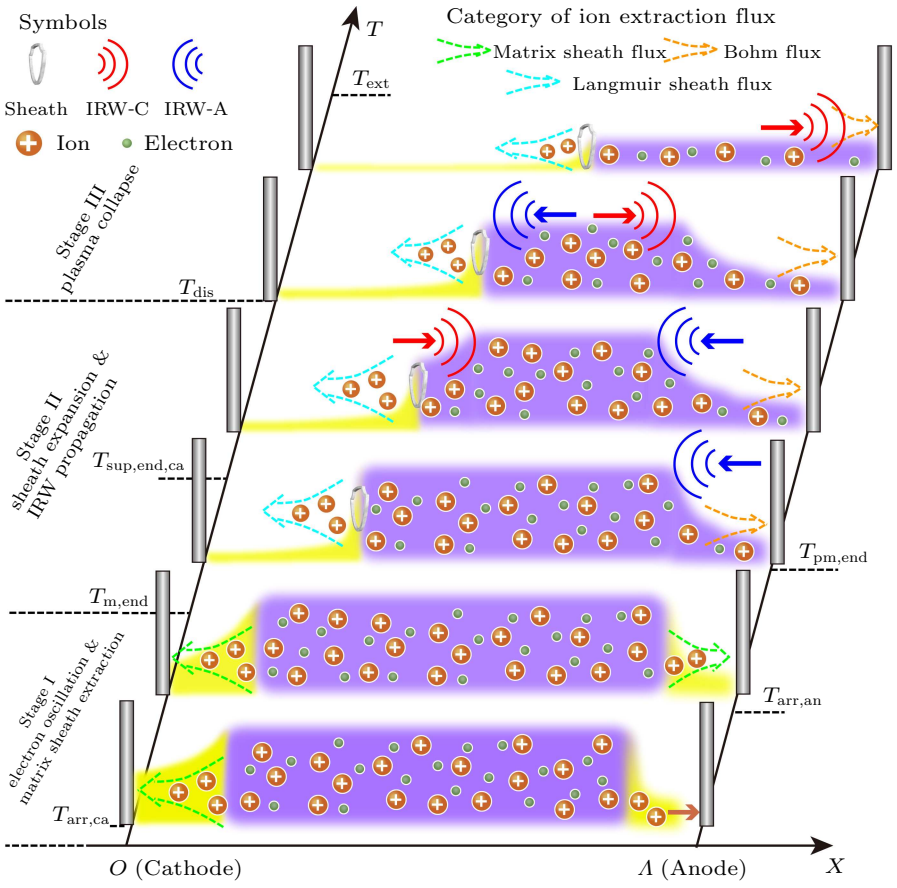


Fig. 10. Schematic of the spatiotemporal evolution of the sheath expansion, IRW propagation and ion extraction fluxes in a 1-D wall-confined decaying plasma under an electrostatic field with considering the IPEG effect, where the purple region stands for the bulk plasma and the yellow region stands for the region filled with ions.

(3) With the increase of the IPEG spacing, the ion extraction time (T_{ext}) generally decreases, while the specific ion extraction time (τ_{ext}) increases, mainly resulting from the decrease of the initial number of ions to be extracted. In contrast to T_{ext}, τ_{ext} may be more appropriate to evaluate the efficiency of the ion extraction process when considering the existence of the IPEGs in practice.

Although the 1-D analytical model developed in this study provides a deeper understanding to the underlying physical mechanisms concerning the IPEG effect on the ion extraction characteristics, which may provide a theoretical guidance for an optimal design of the operating parameters in actual applications, further development of the analytical models taking into account actual operating parameters and geometrical configurations of the ion extraction system is still indispensable in future research. For example, even in a parallel-plate electrostatic extraction system, the initial plasma density distribution may be spatially non-uniform and decreases towards the edge due to the non-uniform energy distribution of the laser beams,[42,43] which may lead to two-dimensional (2-D) effects with non-negligible influences on the ion extraction characteristics; the ions escaping from the upper and lower boundaries of the extraction region may not be neglected provided that the size of the plasma region in the vertical direction is comparable to the length of the electrode, as provided by the PIC simulation results in Refs. [34,41]. On the other hand, in some complex geometries such as M-type or Π-type electrode configurations, the spatiotemporal evolutions of plasma parameters may be quite different from those in a 1-D system. For example, under a Π-type electrode configuration, the electric potential difference between the center region of the plasma and the cathode is less than the externally applied voltage, which suggests that the Π-type electrode configuration can not be simply approximated as a half-plasma-width 1-D parallel-plate electrode configuration as discussed in Ref. [14]. Therefore, an improved analytical model considering the 2-D ion extraction effects needs to be developed in future research based on the present work. Further comparisons with experimental data for different plasmas with different ion masses are also indispensable, especially based on systematic experimental studyies on the ion extraction simulation experimental platform (IEX) established in our lab with a wider operating window of the key plasma parameters such as the initial plasma density and electron temperature.[44]

Appendix A: Brief discussions on the PIC simulation method and parameter selections

The EDIPIC code employs a direct implicit algorithm for advancing the particles, which is a momentum conservation scheme but does not accurately ensure energy conservation.[45,46] As reported in Ref. [46], the numerical heating or cooling effects of the direct implicit algorithm will decrease with decreasing in $v_{th,e}\Delta t/\Delta x$, where $v_{th,e}$, Δt and Δx stand for the electron thermal velocity, time step and grid size, respectively. Numerical modelling under different simulation parameters in Ref. [46] shows that when the grid size (Δx) is less than 3 times the Debye length (λ_D) and $v_{th,e}\Delta t/\Delta x$ is less than 0.3, the ion current and ion density distribution obtained by the direct implicit algorithm are both in good agreement with those obtained by the explicit energy conservation algorithm. In Ref. [45], it is found that when $\Delta x < \lambda_D$ and $\Delta t < 0.2\omega_{pe}$ (where ω_{pe} represents the electron plasma frequency), the direct implicit algorithm, explicit energy conservation algorithm, and the traditional explicit momentum conservation algorithm all converged to the consistent results.

According to Ref. [25], the values of Δx and Δt in this paper are selected as $\Delta x < \lambda_D$ and $\Delta t < \Delta x/v_e$, where v_e is set at 20 times the electron thermal velocity; and thus, $v_{th,e}\Delta t/\Delta x = 0.05$ and $\Delta x/v_e \ll 0.2\omega_{pe}$; that is to say, the preceding selection for Δx and Δt satisfies the criteria specified in Refs. [45–47], which will effectively suppress the numerical heating/cooling effects, and to some extent, ensure the accuracy and stability of the numerical simulations using the EDIPIC code in this study.

In addition, grid independence is also necessary for obtaining accurate modeling results. The calculated values of the ion extraction time (t_{ext}) for the typical case listed in Table 1 under different grid sizes varying from $\Delta x = \lambda_D$ to $\lambda_D/12$ are shown in Fig. A1. It is seen that the value of t_{ext} is negligibly affected when the grid size is smaller than $\lambda_D/10$, e.g., the relative discrepancy of t_{ext} between the cases of $\Delta x = \lambda_D/10$ and $\Delta x = \lambda_D/12$ is lower than 0.1%. Therefore, the selection of $\Delta x = 0.1\lambda_D$ is reasonable for obtaining grid-independent modeling results.

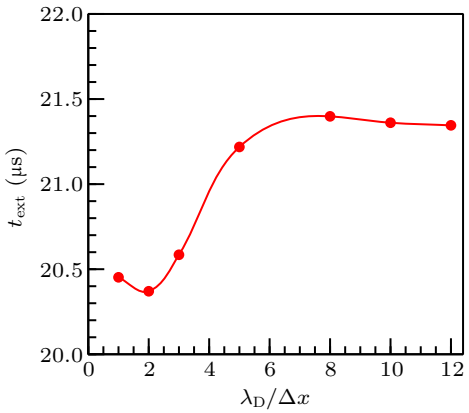


Fig. A1. Variation of the ion extraction time with different grid sizes using the code EDIPIC for the typical case listed in Table 1.

Appendix B: Derivation of matrix sheath thickness on the anode side during the first stage

In this study, it is assumed that: (i) All the electrons in the electron sheet near the anode during the first oscillation

period are absorbed by the anode. This is always valid because the electric field in this region decreases approaching the anode surface, and thus, the electrons are subjected to a stronger attraction force from the anode surface than that from the bulk plasma. Consequently, they will be gradually separated from the electrons in the bulk plasma region and be absorbed by the anode, as described in Ref. [18]. (ii) The sum of lengths of ion sheet near the cathode and anode remains at a constant value of $S_{\mathrm{m,ca}}$. (iii) During the first several oscillation periods, the ion density in the ion sheets and the length of the plasma–electrode gap spacing both remain unchanged. These assumptions are valid under the following two conditions: Firstly, the electrons are not completely exhausted at the anode surface during the first half oscillation period, which corresponds to a critical initial plasma density (n_{c}) derived in Ref. [18]. Only if the initial plasma density (n_0) is larger than n_{c}, the subsequent electron oscillation process can occur. For the typical case listed in Table 1, $n_{\mathrm{c}} = 3.2\times10^{14}$ m^{-3}, which is much smaller than n_0; thus, the electron oscillation and the matrix sheath extraction stage exist as described in Subsection 3.1.1. Secondly, the electron oscillation frequency (ω_{osc}) is required to be much larger than the ion plasma frequency (ω_{pi}) in order that the advance of the ions toward the electrodes during the first several oscillation periods is negligible compared to the motion of electrons. According to Ref. [18], $\omega_{\mathrm{osc}}/\omega_{\mathrm{pi}} = \sqrt{(2D+S_{\mathrm{m,ca}})/\Lambda}\cdot\sqrt{m_{\mathrm{i}}/m_{\mathrm{e}}}$; and for the typical case listed in Table 1, $\omega_{\mathrm{osc}}/\omega_{\mathrm{pi}} = 82.9 \gg 1$.

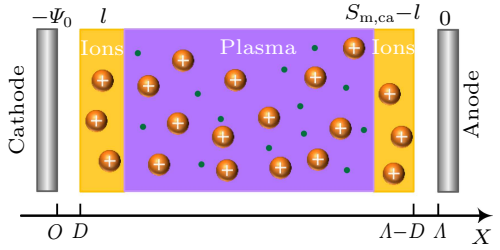


Fig. B1. Schematic of the species spatial distributions in the first several oscillation periods of the electron oscillation process.

As shown in Fig. B1, if we denote the thickness of ion sheet near the cathode as l, the electric field in the bulk plasma region based on the Poisson equation and the corresponding boundary conditions and continuity conditions can be solved and be expressed as

$$E_{\mathrm{bulk}}(l) = \frac{-2\Psi_0 + (2D+S_{\mathrm{m,ca}})(2l-S_{\mathrm{m,ca}})}{2\Lambda}. \tag{B1}$$

Considering an ion located between the bulk plasma and the ion sheet near the anode, the maximum distance that this ion can travel toward the cathode is the maximum thickness of the ion sheet near the anode or the matrix sheath thickness on the anode side ($S_{\mathrm{m,an}}$), which can be obtained according to the kinetic energy theorem as follows:

$$\int_{S_{\mathrm{m,ca}}}^{S_{\mathrm{m,ca}}-S_{\mathrm{m,an}}} E_{\mathrm{bulk}}(l)\mathrm{d}l = 0. \tag{B2}$$

Combining Eqs. (B1) and (B2), $S_{\mathrm{m,an}}$ can be expressed as

$$S_{\mathrm{m,an}} = S_{\mathrm{m,ca}} - \frac{2\Psi_0}{2D+S_{\mathrm{m,ca}}}. \tag{B3}$$

Appendix C: Analyses of the variation trends of $(D+S_{\mathrm{m,ca}})$ and $(D+S_{\mathrm{m,an}})$ with D based on the analytical model in this paper

If we define the functions $f(D) = D+S_{\mathrm{m,ca}}$ and $g(D) = D+S_{\mathrm{m,an}}$, we have the following relationship:

$$f(D) = D+\frac{\Psi_0}{D} \rightarrow f'(D) = 1-\frac{\Psi_0}{D^2} > 1-1 = 0, \tag{C1}$$

$$g(D) = D+\frac{\Psi_0}{D}-\frac{2\Psi_0}{2D+\Psi_0/D}$$

$$\rightarrow g'(D) = \frac{2\Psi_0\left(2D^2-\Psi_0\right)}{\left(2D^2+\Psi_0\right)^2}+1-\frac{\Psi_0}{D^2} > 0+1-1 = 0, \tag{C2}$$

according to Eq. (2) when $D > D_{\mathrm{c}} = (\Psi_0)^{1/2}$. Thus, f and g will both increase with increasing in D since their first derivatives with respect to D are both always positive. While when $D < D_{\mathrm{c}} = (\Psi_0)^{1/2}$, although the value of $S_{\mathrm{m,ca}}$ can be obtained exactly by solving a cubic equation, this exact solution is complicated and difficult for analyzing the variation trend of f or g with D. Therefore, a reasonable simplification for the case of $D < D_{\mathrm{c}}$ is necessary. If we define

$$\eta = \frac{D^2S_{\mathrm{m,ca}}-D^3}{2D^2S_{\mathrm{m,ca}}+3DS_{\mathrm{m,ca}}^2+S_{\mathrm{m,ca}}^3}, \tag{C3}$$

then, based on Eq. (2), we have

$$\eta = \left(-1+\frac{6\Psi_0/D^2}{1-\left(S_{\mathrm{m,ca}}/D\right)^{-1}}\right)^{-1}, \tag{C4a}$$

$$\frac{S_{\mathrm{m,ca}}}{D} = h\left(\Psi_0/D^2\right)+\frac{2\Psi_0/D^2}{h\left(\Psi_0/D^2\right)}-1, \tag{C4b}$$

with

$$h\left(\frac{\Psi_0}{D^2}\right) = \left(\sqrt{-8\left(\frac{\Psi_0}{D^2}\right)^3+9\left(\frac{\Psi_0}{D^2}\right)^2-6\left(\frac{\Psi_0}{D^2}\right)+1}\right.$$
$$\left.-3\left(\frac{\Psi_0}{D^2}\right)+1\right)^{1/3}. \tag{C4c}$$

It is seen from Eqs. (C3) and (C4) that η is a function of (Ψ_0/D^2). With the aid of numerical calculation, η is always no more than 0.05 as shown in Fig. C1. Therefore, an approximation of $(-D^3+D^2S_{\mathrm{m,ca}}) \approx 0$ can be used for the case of $D < D_{\mathrm{c}}$; and consequently, Eq. (2) can be simplified as a quadratic equation in terms of $S_{\mathrm{m,ca}}$ as follows:

$$S_{\mathrm{m,ca}}^2+3DS_{\mathrm{m,ca}}+2D^2-6\Psi_0 = 0$$

$$\rightarrow S_{\mathrm{m,ca}} = -\frac{3D}{2}+\frac{\sqrt{D^2+24\Psi_0}}{2}. \tag{C5}$$

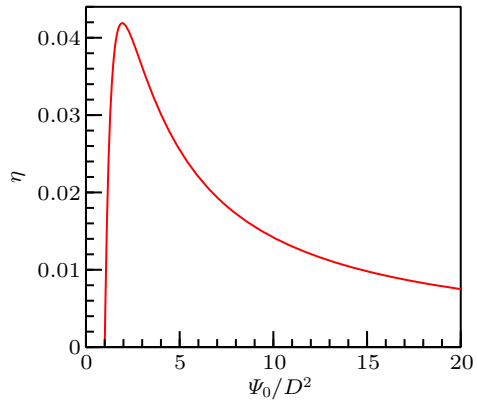


Fig. C1. Variation of η with Ψ_0/D^2 when $D < D_c = (\Psi_0)^{1/2}$.

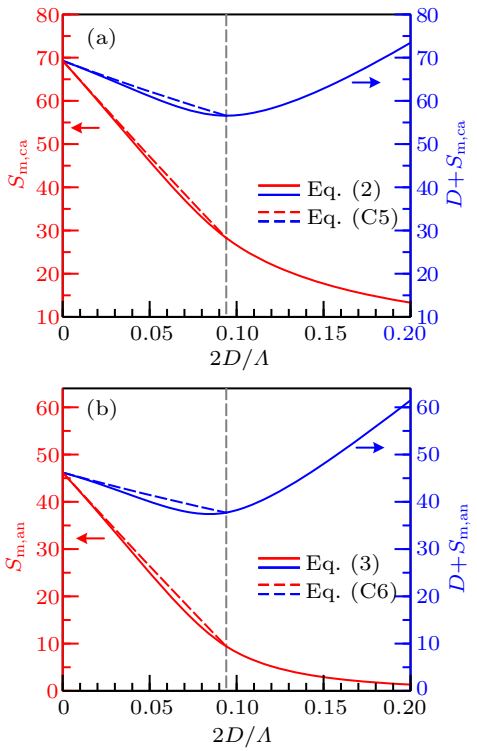


Fig. C2. Comparisons of (a) $S_{m,ca}$, $(D+S_{m,ca})$ and (b) $S_{m,an}$, $(D+S_{m,an})$ between the values obtained by the original analytical model [Eqs. (2) and (3)] and the corresponding approximate formulae [Eqs. (C5) and (C6)]. The grey dashed line is located at $2(\Psi_0)^{1/2}/\Lambda$.

By introducing Eq. (C5) into Eq. (3), the approximated value of $S_{m,an}$ can be written as

$$S_{m,an} = -\frac{3D}{2} + \frac{\sqrt{D^2+24\Psi_0}}{2} - \frac{4\Psi_0}{\sqrt{D^2+24\Psi_0}+D}. \quad \text{(C6)}$$

Based on Eqs. (C5) and (C6), we have

$$f(D) = -\frac{D}{2} + \frac{\sqrt{D^2+24\Psi_0}}{2}$$
$$\rightarrow f'(D) = \frac{1}{2}\left(\frac{D}{\sqrt{D^2+24\Psi_0}} - 1\right) < 0, \quad \text{(C7)}$$
$$g(D) = -\frac{D}{2} + \frac{\sqrt{D^2+24\Psi_0}}{2} - \frac{4\Psi_0}{\sqrt{D^2+24\Psi_0}+D}$$
$$\rightarrow g'(D) = -\frac{8\Psi_0}{D\sqrt{D^2+24\Psi_0}+D^2+24\Psi_0} < 0, \quad \text{(C8)}$$

for the case of $D < D_c = (\Psi_0)^{1/2}$. Thus, it can be seen that f and g will both decrease with the increase of D since their first derivatives with respect to D are both always negative as shown in Figs. C2(a) and C2(b), respectively. The approximated values of $S_{m,ca}$ and $S_{m,an}$ obtained by Eqs. (C5) and (C6) agree well with those obtained by Eqs. (2) and (3) with maximum relative discrepancies of 3.7% and 9.7%, respectively. Correspondingly, the variations of $(D+S_{m,ca})$ and $(D+S_{m,an})$ show nonmonotonic variation trends with increasing in D. It should be noted that the local minimum point of $(D+S_{m,an})$ in Fig. C2(b) is not exactly at $D=(\Psi_0)^{1/2}$ with a relative discrepancy of 10.3%. This is because the predicted value of $S_{m,an}$ by Eq. (C6) deviates slightly from that predicted by the original analytical model [Eq. (3)].

Acknowledgement

Project supported by the National Key Laboratory of Particle Transport and Separation Technology (Grant No. WZKF-2024-2).

References

[1] Lieberman M A 1989 *J. Appl. Phys.* **66** 2926
[2] Riemann K U and Daube T 1999 *J. Appl. Phys.* **86** 1202
[3] Daube T, Meyer P, Riemann K U and Schmitz H 2002 *J. Appl. Phys.* **91** 1787
[4] Widner M, Alexeff I, Jones W D and Lonngren K E 1970 *Phys. Fluids* **13** 2532
[5] Chen F F 1982 *Phys. Fluids* **25** 2385
[6] Li H P, Wang P, Wang X, You W, Chai J J and Li Z Y 2015 *High Voltage Eng.* **41** 2825 (in Chinese)
[7] Li H P, Wang X, Wang P, Chai J J and Li Z X 2016 *High Voltage Eng.* **42** 706 (in Chinese)
[8] Ogura K, Arisawa T and Shibata T 1992 *Jpn. J. Appl. Phys.* **31** 1485
[9] Nishio R, Yamada K, Suzuki K and Wakabayashi M 1995 *J. Nucl. Sci. Technol.* **32** 180
[10] Kurosawa H, Hasegawa S and Suzuki A 2002 *J. Appl. Phys.* **91** 4818
[11] Singh P, Sridhar G and Maiti N 2023 *IEEE Trans. Plasma Sci.* **51** 35
[12] Yamada K, Tetsuka T and Deguchi Y 1991 *J. Appl. Phys.* **69** 8064
[13] Lu X Y, Yuan C, Zhang X Z and Zhang Z Z 2020 *Chin. Phys. B* **29** 045201
[14] Wang Y T, Chen J, Li H P, Jiang D J and Zhou M S 2021 *Jpn. J. Appl. Phys.* **60** SAAB05
[15] Matsui T, Tsuchida K, Tsuda S, Suzuki K and Shoji T 1996 *Phys. Plasmas* **3** 4367
[16] Matsui T, Tsuchida K, Tsuda S, Suzuki K and Shoji T 1997 *J. Nucl. Sci. Technol.* **34** 923
[17] Ohzu A, Suzuki Y, Maruyama Y and Arisawa T 2000 *Phys. Plasmas* **7** 770
[18] Wang Y T, Luo L Y, Li H P, Jiang D J and Zhou M S 2022 *Acta Phys. Sin.* **71** 232801 (in Chinese)
[19] Yamada K and Tetsuka T 1994 *J. Nucl. Sci. Technol.* **31** 301
[20] Murakami M, Ueshima Y and Nishihara K 1993 *Jpn. J. Appl. Phys.* **32** L1471
[21] Zhidkov A G 1998 *Phys. Plasmas* **5** 541
[22] Zhu H L and Wang D W 2003 *Atom. Energy Sci. Technol.* **37** 467 (in Chinese)
[23] Okano K 1992 *J. Nucl. Sci. Technol.* **29** 601
[24] Murakami M and Nishihara K 1993 *Phys. Fluids B* **5** 3441
[25] Wang Y T, Sun X L, Luo L Y, Zhang Z M, Li H P, Jiang D J and Zhou M S 2023 *Chin. Phys. B* **32** 095201
[26] Vitello P, Cerjan C and Braun D 1992 *Phys. Fluids B* **4** 1447

[27] Chen J, Xiang J Q, Guo H, Li H P, Chen X, Wang P, Chai J J, Jiang D J and Zhou M S 2017 *High Voltage Eng.* **43** 1830 (in Chinese)
[28] Chen J, Fu T Z, Guo H, Li H P, Jiang D J and Zhou M S 2019 *Plasma Sci. Technol.* **21** 045402
[29] Chen J, Khrabrov A V, Wang Y T, Li J, Li H P, Jiang D J and Zhou M S 2020 *Plasma Sources Sci. Technol.* **29** 025010
[30] Allen J E and Andrews J G 1970 *J. Plasma Phys.* **4** 187
[31] Khrabrov A V, Kaganovich I D, Chen J and Guo H 2020 *Phys. Plasmas* **27** 123512
[32] Litvinov I I 1997 *J. Russ. Laser Res.* **18** 87
[33] Chen J, Li J, Li H P, Jiang D J and Zhou M S 2020 *High Voltage Eng.* **46** 729 (in Chinese)
[34] Wang Y T 2024 *Studies on the Transport Mechanisms of the Charged Particles in Low-pressure Bounded Plasmas* (Ph.D. Dissertation) (Beijing: Tsinghua University) (in Chinese)
[35] Mahdieh M H and Gavili A 2003 *Plasma Sources Sci. Technol.* **12** 513
[36] Yamada K, Tetsuka T and Deguchi Y 1990 *J. Appl. Phys.* **67** 6734
[37] Yamada K, Tetsuka T and Deguchi Y 1991 *J. Appl. Phys.* **69** 6962
[38] Yamada K, Okada H, Tetsuka T and Yoshioka K 1993 *J. Nucl. Sci. Technol.* **30** 143
[39] Sydorenko D 2006 *Particle-in-cell simulations of electron dynamics in low pressure discharges with magnetic fields* (Ph.D. Dissertation) (Saskatchewan: The University of Saskatchewan)
[40] Xiong J G and Wang D W 2000 *Acta Phys. Sin.* **49** 2420 (in Chinese)
[41] Singh P, Sridhar G and Maiti N 2023 *Curr. Appl. Phys.* **47** 30
[42] Yan M, Wang D W, Ying C T and Zhu X H 1994 *Nucl. Sci. Eng.* **14** 271 (in Chinese)
[43] Chen X, Lu X Y and Cai L 2024 *AIP Adv.* **14** 085212
[44] Chen J, Liu Z Q, Guo H, Li H P, Jiang D J and Zhou M S 2018 *Acta Phys. Sin.* **67** 182801 (in Chinese)
[45] Wang H Y, Jiang W, Sun P and Kong L B 2014 *Chin. Phys. B* **23** 035204
[46] Sun H, Banerjee S, Sharma S, Powis A T, Khrabrov A V, Sydorenko D, Chen J and Kaganovich I D 2023 *Phys. Plasmas* **30** 103509
[47] Donkó Z, Derzsi A, Vass M, Horváth B, Wilczek S, Hartmann B and Hartmann P 2021 *Plasma Sources Sci. Technol.* **30** 095017